XV Bi-power law correlations for sediment transport in pressure driven channel flows

Direct numerical simulation (DNS) can be used to extract information implicit in the equations of fluid-particle motion. We have investigated the lift-off of a single particle and many particles in pressure driven flows by 2D DNS (N.A. Patankar, Huang, Ko & Joseph 2001a, Ko, N.A. Patankar & Joseph 2001, Joseph, & Ocando 2001, Choi & Joseph 2001, N.A. Patankar, Ko, Choi & Joseph 2001b). We show that the lift-off of single particles and many particles in horizontal flows follow laws of similarity, power laws, which may be obtained by plotting simulation data on log-log plots. Power laws emerge as in the case of Richardson-Zaki correlations for fluidization by drag. Power laws also emerge from the experimental data from STIM-LAB (Patankar, Joseph, Wang, Barree, Conway & Asadi 2002 and Wang, Joseph, Patankar, Conway & Barree 2002). These engineering correlations for lift-off can be used to predict proppant placement in hydraulic fracturing.

The fracturing industry makes extensive use of numerical simulation schemes based on models and programmed to run on PC's to guide field operations. These simulations are used to predict how the fracture crack opens and closes and how proppant is transported in the crack. Commercial packages dealing with these problems and propriety packages developed by oil service companies are used extensively. These numerical schemes solve the average equations for the fluid and the proppant phases. The solid and the fluid are considered as inter-penetrating mixtures, which are governed by conservation laws. Interaction between the inter-penetrating phases is modeled. Models for drag and lift forces on the particles must be used for fluid-proppant interaction. Models for the drag force on particles in solid-liquid mixtures is a complicated issue and usually rely on the well-known Richardson-Zaki 1954 correlation. Models for lift forces in mixtures are much less well developed than models for drag. Therefore, none of the packages model the all important levitation of proppants by hydrodynamic lift. The power law models we are developing from DNS and experiments may be incorporated in the model-based simulation techniques similar to the model for drag.

- ▪ **Analogy between fluidization by drag and lift**

(a)

$g \downarrow$

Uniform fluid flow

(b)
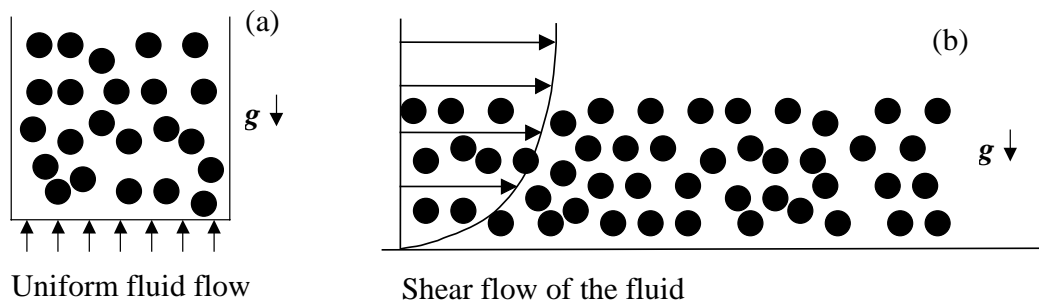
$g \downarrow$

Shear flow of the fluid

Figure XV.1. (a) Heavy particles fluidized by uniform fluid flow from the bottom of a vertical column. (b) Heavy particles fluidized by lift due to shear flow of the fluid in a horizontal channel. Gravity acts vertically downwards.

Fluidization by drag and shear is depicted in the cartoons in figure XV.1. In figure XV.1a the fluid enters at the bottom of a vertical column at a uniform fluidization velocity. At equilibrium, the drag exerted by the fluid balances the net buoyant weight of the particles. The particle bed

acquires a height corresponding to the average particle fraction ϕ. When the fluidizing velocity is increased the particle bed expands. Richardson & Zaki 1954 did experiments with different fluids, particles and fluidization velocities. They plotted their data in log-log plots; miraculously this data fell on straight lines whose slope and intercept could be determined. This showed that the variables follow power laws; a theoretical explanation for this outstanding result has not been proposed. After processing the data Richardson & Zaki (RZ) found that

$$V_\phi = V_0 \, [1\text{-}\phi]^{n(R_0)} \tag{XV.1}$$

where V_ϕ is the fluidization velocity at the column entrance or the composite velocity. V_0 is the "blow out" velocity, when $\phi = 0$; when $V_\phi > V_0$ all the particles are blown out of the bed. Clearly $V_\phi < V_0$ for a fluidized bed. For fluidization columns with large cross section in comparison to the particle size, the RZ exponent $n(R_0)$ depends on the Reynolds number $R_0 = V_0 d/\nu$ only, where d denotes the particle size e.g. diameter of a spherical particle and ν is the kinematic viscosity of the fluid. The power law in the RZ case is an example of what Barenblatt 1996 calls "incomplete self similarity" because the power itself depends on the Reynolds number, a third parameter. Pan, Joseph, Bai, Glowinski & Sarin 2001 carried out 3D DNS of the fluidization of 1204 spheres and obtained a correlation in agreement with (XV.1). The Richardson-Zaki correlation gives different expressions for n for different values of R_0. In the appendix R.D. Barree presents a way of representing the various expressions for n by a single continuous function.

(XV.1) describes the complicated dynamics of fluidization by drag. The single particle fluidization velocity plays a key role in obtaining the fluidization velocity of concentrated suspensions. An expression for the drag force $F_d(1)$ on a single isolated particle in an infinite ambient of the fluid is given by a drag law, e.g.

$$F_d(1) = \begin{cases} 3\pi\eta dV_0, & \text{laminar} \\ 0.055\pi\rho_f d^2 V_0^2, & \text{turbulent} \end{cases} \tag{XV.2}$$

where η is the fluid dynamic viscosity, ρ_f is the fluid density and spherical particles are considered. In a fluidized bed the total force F acting on a particle is (Foscolo & Gibilaro 1984, Joseph 1990)

$$F(\varepsilon, R_0) = F_d(\varepsilon) - F_B(\varepsilon), \tag{XV.3}$$

where ε is the fluid fraction, $F_d(\varepsilon)$ is the drag on a single particle in the fluid-particle mixture and $F_B(\varepsilon)$ is the effective buoyant weight of a particle in the suspension. We have, $F_B(\varepsilon) = V_p(\rho_p - \rho_c)g = \varepsilon V_p(\rho_p - \rho_f)g = \varepsilon F_B(1)$, where ρ_p is the particle density, V_p is the volume of the particle, g is the gravitational acceleration, $F_B(1)$ is the buoyant weight of an isolated particle and $\rho_c = \varepsilon\rho_f + \phi\rho_p$ is the effective or composite density of the fluid-particle mixture. At steady conditions

$$\begin{aligned} &F(\varepsilon, R_0) = 0, \\ &i.e.\, F_d(\varepsilon) = F_B(\varepsilon) = \varepsilon F_B(1), \\ &i.e.\, F_d(\varepsilon) = \varepsilon F_d(1). \end{aligned} \tag{XV.4}$$

For spherical particles, (XV.1), (XV.2) and (XV.4) give

$$\left[\pi d^3 \middle/ 6\right]\left[\rho_p - \rho_f\right]g = \begin{cases} 3\pi\eta dV_\phi \varepsilon^{-n(R_0)}, & \text{laminar} \\ 0.055\pi\rho_f d^2 V_\phi^2 \varepsilon^{-2n(R_0)}, & \text{turbulent} \end{cases}$$

or $\hspace{9cm}$, $\hspace{1cm}$ (XV.5)

$$R_G = \begin{cases} 18\varepsilon^{-n(R_0)}R_\phi, & \text{laminar} \\ \left[\varepsilon^{-n(R_0)}R_\phi\right]^2, & \text{turbulent} \end{cases}$$

where $R_G = \rho_f[\rho_p - \rho_f]gd^3 \middle/ \eta^2$ represents the Reynolds number based on the sedimentation velocity scale $V_G = [\rho_p - \rho_f]gd^2 \middle/ \eta$ and $R_\phi = \rho_f V_\phi d \middle/ \eta$. (XV.5) is another form of the correlation for fluidization by drag and can be written as

$$R_G = a(R_0)R_\phi^{p(R_0)}\varepsilon^{q(R_0)}. \hspace{3cm} \text{(XV.6)}$$

Figure XV.1b shows the fluidization of particles by shear flow observed in experiments and numerical simulations. At equilibrium the average lift exerted by the fluid should balance the net buoyant weight of the particles. When the applied shear rate is increased the particle bed expands. This is similar to the fluidization by drag where the mechanism for bed expansion is different. Correlations analogous to (XV.6) may be expected for fluidization by shear. In that case a Reynolds number based on the applied shear rate should be defined instead of R_ϕ. The prefactor and the exponents may be determined from experimental or numerical data.

- ## Direct numerical simulation (DNS) of solid-liquid flows

Choi & Joseph 2001 and N.A. Patankar *et. al* 2001b used the ALE scheme to study the fluidization by lift of 300 circular particles in a plane Poiseuille flow by direct numerical simulation.

Particles are initially placed at the bottom of a periodic channel of height H_1 in a close packed ordered configuration (figure XV.2). The flow is driven by an external pressure gradient. At steady condition, the particle bed reaches a constant height (figure XV.2). The height of the clear fluid region above the particle bed is H_2. From non-dimensional analysis we get

$$R_G = f\left(R, \varepsilon, \varepsilon_{\max}, \frac{H_1}{d}\right),$$

where $\hspace{9cm}$ (XV.7)

$$\varepsilon = 1 - \frac{N\pi d^2}{4[H_1 - H_2]l}, \varepsilon_{\max} = 1 - \frac{N\pi d^2}{4H_1 l},$$

where the shear Reynolds number is $R = \dfrac{\rho_f \dot{\gamma}_w d^2}{\eta}$, the gravity Reynolds number or non-dimensional lift is $R_G = \dfrac{\rho_f(\rho_p - \rho_f)gd^3}{\eta^2}$, N is the number of particles, l is the channel length, ε is the average fluid fraction in the particle bed whose height is $(H_1 - H_2)$ and ε_{max} is the fluid fraction in the particle bed if the particles occupy the entire height of the channel i.e. if $H_2 = 0$.
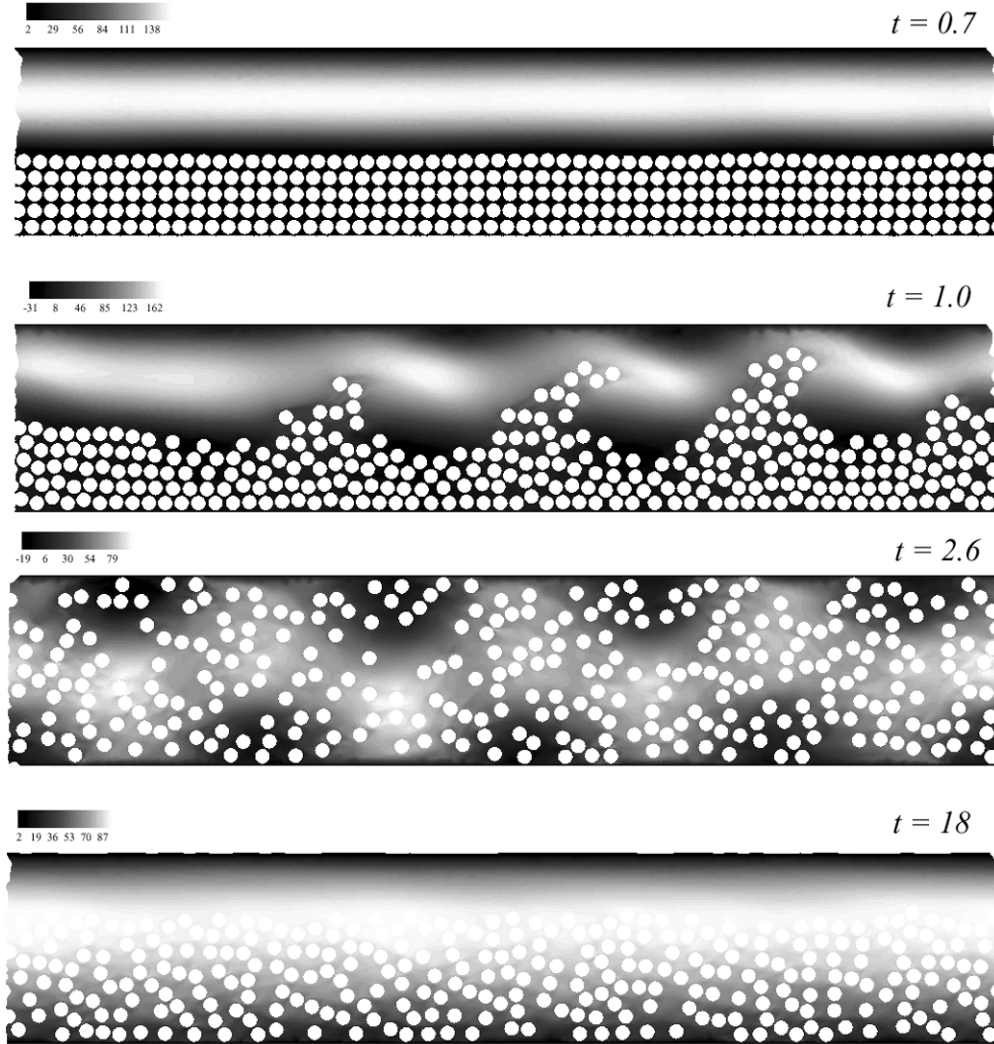
Figure XV.2. (N.A. Patankar, Ko, Choi & Joseph 2001b) Lift-off of 300 heavy particles in a plane pressure driven flow of a Newtonian fluid, Re = 1800. Contour plot of the horizontal velocity component is shown.

During the simulations ε_{max} and H_1/d were constant (N.A. Patankar *et al.* 2001b, Choi & Joseph 2001). In that case, R_G is a function of R and ε only. N.A. Patankar *et al.* 2001b obtained the following correlation

$$R_G = 3.27 \times 10^{-4} \varepsilon^{-9.05} R^{1.249}$$

or (XV.8)

$$R_G = 3.27 \times 10^{-4} \left[\frac{\varepsilon_{max} - H_2/H_1}{1 - H_2/H_1} \right]^{-9.05} R^{1.249}.$$

The correlation above is of the same form as that expected from (XV.6). This shows that fluidization of slurries by lift also falls into enabling correlations of the RZ type and the above correlation by N.A. Patankar *et al.* 2001b could be called a Richardson-Zaki type of correlation for fluidization by lift. Lift results for fluidized slurries are power laws in appropriate

dimensionless parameters. These power laws are in the form of engineering type correlations; to use them in applications we need rules for converting two- to three-dimensional results. The goal of our future work is to generate power laws for engineering applications by processing results of simulations in 3D just as we have done in 2D.

The DNS results are in agreement with the expected power law form in (XV.6) from the analogy between fluidization by drag and shear. In the next sections we present the experimental results for proppant transport to verify the prediction of power laws from DNS (N.A. Patankar, *et al.* 2002, Wang, *et al.* 2002).

- ▪ **Experimental setup**

Kerns, Perkins, and Wyant 1959 reported the earliest experimental investigation of proppant transport in narrow slots. STIM-LAB did more experiments to better understand the processes involved in proppant transport by water and other thin fluids. We have analyzed the data obtained from their experiments. The apparatus used by STIM-LAB was constructed so that the transport of proppant in a horizontally oriented slot could be observed. A schematic of the apparatus is shown in figure XV.3.
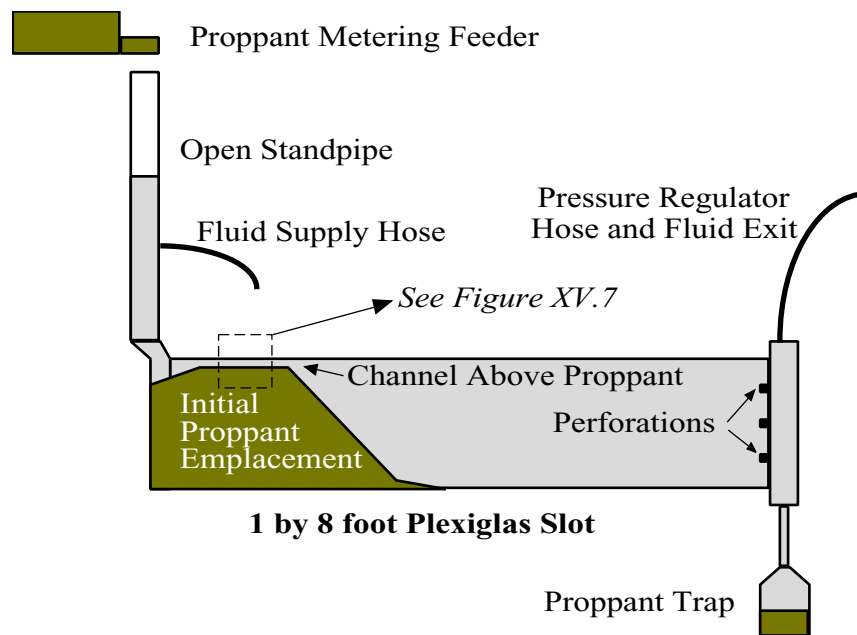

Figure XV. 3. (N.A. Patankar et al. *2002) The experimental setup for proppant transport. Proppant and fluid are added at the left where they enter over the full height of the slot. Materials exit at the right through perforations.*

Proppant can be added at a constant rate and water flow rate is also constant. Proppant and water enter the 7.94 mm wide slot through an open end that is 30.5 cm tall. The proppant and water then move through the 2.44 m length of the slot where they exit via three 8 mm perforations spaced 7.62 cm apart on the 30.5 cm tall end of the slot. The proppant and water flow rates were varied, proppants of varying size and density were added and water at different

temperatures was used. Observations were recorded and portions of the experiments were video taped.

The evolution of the proppant bed in the experiments is well described in figure XV.4. The portion shown in figure XV.4 is marked in figure XV.3. In the steady state there is an initial development length (see figure XV.3) followed by a flat bed region shown in figure XV.4 and marked in figure XV.3. There are three distinct zones in the flat bed region. The bottom part of the bed is immobile; it is a stationary porous medium that supports liquid throughput that might be modeled by Darcy's law. Above the immobile bed is a mobile bed in which particles move by sliding and rolling or advection after suspension or a combination of these modes. Above the mobile bed is the clear fluid zone. At steady state the volumetric fluid flow rate Q_f and the volumetric proppant flow rate Q_p in and out of this region are constant. At steady state, these are equal to the rate at which the fluid and proppant are injected in the slot.

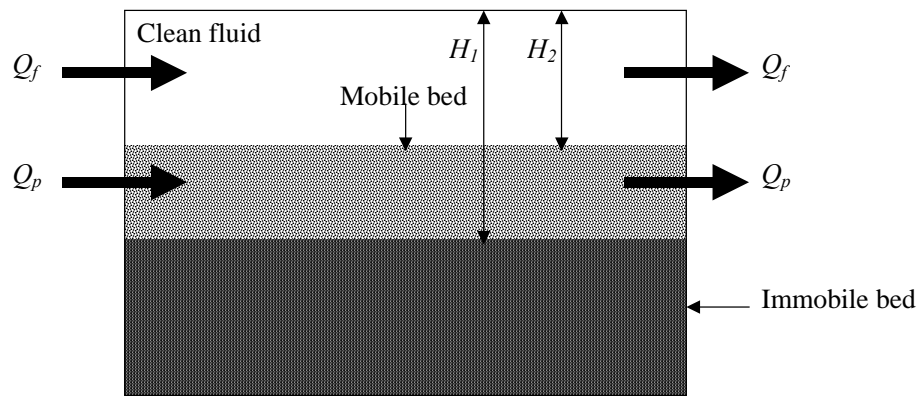Clean fluid — H_1 — H_2 — Q_f — Q_f — Mobile bed — Q_p — Q_p — Immobile bed

Figure XV.4. (N.A. Patankar et al. 2002) Proppant transport in thin fluids at steady state conditions. In Case 1 only fluid is pumped, $Q_P = 0$, $H_1 = H_2$; the particles are immobile. In Case 2 proppants are also injected, $Q_P \neq 0$, $H_1 \neq H_2$; there is a mobile bed of height $H_1 - H_2$. The channel width W = 7.94 mm.

STIM-LAB carried out two types of experiments looking at the transport of proppants in thin fluids. In Case 1 only fluid is pumped, $Q_P = 0$, $H_1 = H_2$; the particles are immobile. We call case 1 *erosion case*. In Case 2 proppants are also injected, $Q_P \neq 0$, $H_1 \neq H_2$; there is a mobile bed of height $H_1 - H_2$. We call case 2 *bed load transport case*. The channel width $W = 7.94$ mm. A simplified description of the experiment is that a bed of proppant is eroded by the flow of water. When proppant is not injected as in Case 1, the faster the flow of water the deeper is the channel above the proppants. We are seeking to predict the height above the channel for the given fluid flow rate. In Case 2, we seek to predict both the clear fluid height as well as the mobile bed height as functions of Q_f and Q_p. In the experiments the fluid and the proppant flow rates are controlled and the heights H_1, H_2 are measured.

In the DNS of 300 particles reported by Choi & Joseph 2001 and N.A. Patankar *et al.* 2001b (figure XV.2), we have a set up similar to that in figure XV.4. The value of H_1 in figure XV.4 is equivalent to the height of the channel in the simulations. In the simulations, data is obtained for a fixed value of H_1/d. This is not the case with the experimental data.

▪ Experimental correlations for sediment transport

Dimensionless parameters

The dimensionless parameters in this problem are listed below:

Gravity Reynolds number

$$R_G = \frac{\rho_f[\rho_p - \rho_f]gd^3}{\eta^2}.$$ (XV.9)

Gravity Reynolds number for the fluid

$$\lambda = \frac{\eta/\rho_f}{W^{3/2}\sqrt{g}} \cdot (\frac{1}{\lambda^2} = \frac{\rho_f^2 gW^3}{\eta^2})$$ (XV.10)

Note that $1/\lambda$ can be viewed as the Reynolds number based on a velocity scale $V \sim \sqrt{gW}$ and length scale W.

Fluid Reynolds number based on channel width

$$R_f = \frac{\rho_f \tilde{V}W}{\eta} = \frac{\rho_f Q_f}{W\eta}, \text{ where } \tilde{V} = \frac{Q_f}{W^2}.$$ (XV.11)

Proppant Reynolds number based on channel width

$$R_p = \frac{\rho_p \overline{V}W}{\eta} = \frac{\rho_p Q_p}{W\eta}, \text{ where } \overline{V} = \frac{Q_p}{W^2}.$$ (XV.12)

Particle diameter/channel width: d/W.

Height of bed/channel width: H/W.

Power law correlations for the erosion case (Patankar et al. 2002)

The erosion case: $H_1 = H_2 = H$ finds the critical condition of the initial motion of the proppant. Only fluid is injected in the channel. The particle bed is immobile. There is an equilibrium value of H corresponding to a given fluid flow rate. When the fluid flow rate is increased beyond the critical value for a given initial height H, the proppants are eroded from the bed and washed out until a new equilibrium height H of the clear fluid region above an immobile bed is achieved for the new flow rate.

Table XV.1 gives the data from these experiments. Figure XV.5 shows a plot of H/W vs. R_f at different values of R_G.
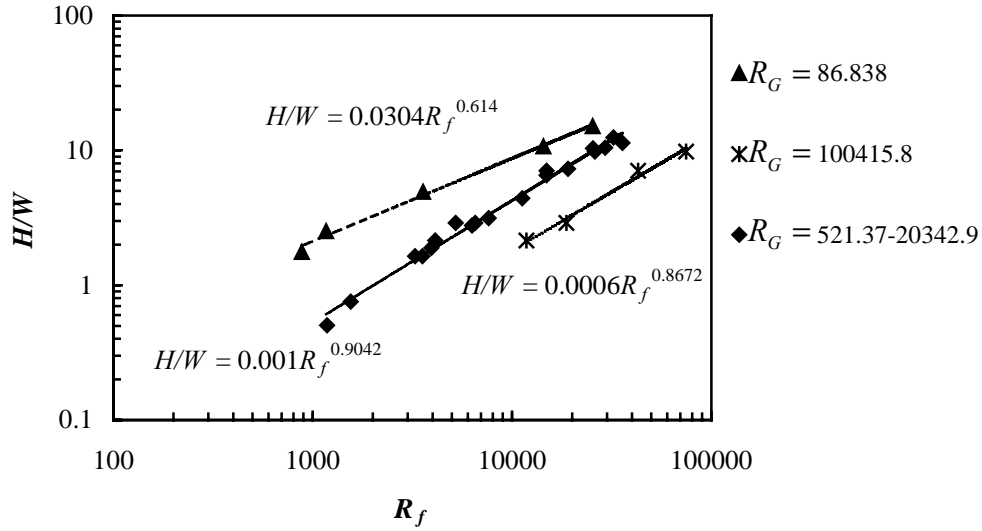
$H/W = 0.0304 R_f^{0.614}$

$\blacktriangle R_G = 86.838$

$\text{\textasteriskcentered} R_G = 100415.8$

$\blacklozenge R_G = 521.37\text{-}20342.9$

$H/W = 0.0006 R_f^{0.8672}$

$H/W = 0.001 R_f^{0.9042}$

Figure XV.5. Plot of H/W vs. R_f at different values of R_G on a logarithmic scale.

Proppants	d (cm)	H (cm)	η (gm/cm-s)	ρ_f (gm/cc)	Q_f (cc/s)	ρ_p (gm/cc)	R_G	$\tilde{V}$ (cm/s)	R_f	H/W
	0.034212	1.7	0.01115	0.999	36.778	2.65	521.1645	58.37416	4184.12	2.141732
60/40	0.034212	2.3	0.01115	0.999	58.289	2.65	521.1645	92.51649	6631.36	2.897638
Brady	0.034212	5.6	0.01115	0.999	133.295	2.65	521.1645	211.5662	15164.55	7.055118
	0.034212	7.8	0.01115	0.999	232.588	2.65	521.1645	369.1644	26460.80	9.826772
	0.056043	2.3	0.01115	0.999	46.556	2.65	2290.822	73.89383	5296.48	2.897638
20/40	0.056043	5.2	0.01115	0.999	133.106	2.65	2290.822	211.2663	15142.90	6.551181
Ottawa	0.056043	8.2	0.01115	0.999	227.542	2.65	2290.822	361.1554	25886.49	10.33071
	0.06	1.4	0.01115	0.999	7.885	1.05	86.83778	12.5151	897.05	1.76378
20/40	0.06	2	0.01115	0.999	10.409	1.05	86.83778	16.5212	1184.19	2.519685
Light	0.06	3.9	0.01115	0.999	31.92	1.05	86.83778	50.66353	3631.42	4.913386
Beads	0.06	8.5	0.01115	0.999	128.438	1.05	86.83778	203.8572	14611.89	10.70866
	0.06	12	0.01115	0.999	226.217	1.05	86.83778	359.0523	25735.84	15.11811
	0.094946	1.5	0.01	0.998	31.542	2.73	14513.72	50.06356	3997.08	1.889764
16/20	0.094946	2.2	0.01	0.998	50.467	2.73	14513.72	80.10138	6395.30	2.771654
Carbolite	0.094946	9.9	0.01	0.998	258.642	2.73	14513.72	410.5174	32775.74	12.47244
	0.094946	1.7	0.00378	0.972	36.778	2.73	100415.8	58.37416	12008.41	2.141732
16/20	0.094946	2.3	0.00378	0.972	58.289	2.73	100415.8	92.51649	19031.98	2.897638
Carbolite	0.094946	5.6	0.00378	0.972	133.295	2.73	100415.8	211.5662	43522.25	7.055118
	0.094946	7.8	0.00378	0.972	232.588	2.73	100415.8	369.1644	75942.48	9.826772

Proppants	d (cm)	H (cm)	η (gm/cm-s)	ρ_f (gm/cc)	Q_f (cc/s)	ρ_p (gm/cc)	R_G	$\tilde{V}$ (cm/s)	R_f	H/W
(continued)										
16/30	0.088437	0.4	0.01115	0.999	10.535	3.45	13363.76	16.72119	1198.53	0.503937
Banrite	0.088437	0.6	0.01115	0.999	13.878	3.45	13363.76	22.02721	1578.85	0.755906
	0.088437	1.3	0.01115	0.999	29.145	3.45	13363.76	46.25904	3315.71	1.637795
	0.088437	3.5	0.01115	0.999	100.681	3.45	13363.76	159.8012	11454.08	4.409449
	0.088437	8.3	0.01115	0.999	261.796	3.45	13363.76	415.5234	29783.50	10.45669
	0.109021	1.3	0.01015	0.998	28.955	2.65	20342.9	45.95747	3615.03	1.637795
12/20	0.109021	2.5	0.01015	0.998	62.137	2.65	20342.9	98.62404	7757.81	3.149606
Badger	0.109021	5.8	0.01015	0.998	155.185	2.65	20342.9	246.3101	19374.85	7.307087
	0.109021	9	0.01015	0.998	290.814	2.65	20342.9	461.5809	36308.13	11.33858

Table XV.1: Data from experiments on the initiation of sediment motion (Erosion Case).

In the erosion case, three dimensionless parameters R_f, H/W, and R_G enter the power law correlation

$$\frac{H}{W} = a(R_G)R_f^{m(R_G)} \tag{XV.13}$$

where *a* and *m* are function of R_G.[1] The values of *a* and *m* may be regarded as constants for $521.37 \le R_G \le 20342.9$ (table XV.2).

R_G	86.838	521.37 — 20342.9	100415.8
a	0.0304	0.001	0.0006
m	0.614	0.90432	0.8672

Table XV.2. The prefactor a(R_G) and exponent m(R_G) in the power law correlations for the erosion case.

Bi-power law correlations for the bed load transport case (Wang et al. 2002)

Bed load transport is another name for the transport of sediments. In bed load transport cases, both fluids and proppants play important role in determining H_1 and H_2. Therefore we seek correlations for H_1/W and H_2/W in terms of R_f and R_p with the coefficients as functions of R_G

---

[1] Shield's (1936) curve also gives the critical condition for the initiation of sediment motion. The Shields parameter

S is defined as: $S = \dfrac{\tau}{[\rho_p - \rho_f]gd}$, where τ is a measure of the shear stress on the particle bed. If we take

$\tau = \eta \tilde{V}/W$, then $S = \dfrac{\eta \tilde{V}}{[\rho_p - \rho_f]gd^2} = \dfrac{R_f[d/W]}{R_G}$. From the Shield's 1936 curve one obtains (see also, Vanoni

1975) $S = f_s (\sqrt{R_f}[d/W])$. (XV.13), applicable for proppant transport in narrow channels, has W/H as another

parameter. Nothing close to the bi-power law correlations has been put forward for sediment transport.

and λ. To create correlations, we need data and a data structure. An example of the way the data is structured for processing correlations is given for 20/40 Ottawa in water in table XV.3.

ρ_f: 1.0gm/cc, ρ_p: 2.65gm/cc, d: 0.06cm, η: 0.01poise, W: 0.79375cm, R_G: 3496.28, λ: 0.000451.

Q_p (cc/s)	Q_f (cc/s)	R_f	R_p	H_1 (cm)	H_2 (cm)	H_1/W	H_2/W
40	244.1	30752.76	13354.33	2.3	0.8	2.897638	1.007874
45.7	242.9	30601.57	15257.32	2.6	0.7	3.275591	0.88189
28.6	250.4	31546.46	9548.346	2.3	1	2.897638	1.259843
11.4	249.8	31470.87	3805.984	2.4	1.5	3.023622	1.889764
11.4	313.5	39496.06	3805.984	3	2.1	3.779528	2.645669
34.3	304.7	38387.4	11451.34	2.9	1.5	3.653543	1.889764
11.4	314.8	39659.84	3805.984	3.1	2.3	3.905512	2.897638
45.7	303.4	38223.62	15257.32	3	1.4	3.779528	1.76378
40	305.3	38462.99	13354.33	3	1.5	3.779528	1.889764
28.6	306	38551.18	9548.346	2.9	1.6	3.653543	2.015748
22.8	306	38551.18	7611.969	2.8	1.7	3.527559	2.141732
17.1	315.4	39735.43	5708.976	3.1	2	3.905512	2.519685
5.7	314.2	39584.25	1902.992	3.5	2.9	4.409449	3.653543
2.9	313.5	39496.06	968.189	4.1	3.6	5.165354	4.535433
1.4	312.9	39420.47	467.4016	5.1	5	6.425197	6.299213
0.4	311.6	39256.69	133.5433	5.8	5.7	7.307087	7.181102

Table XV.3: Experimental data for the bed load transport case with 20/40 Ottawa and water.

We look for correlations in the bi-power law form with five dimensionless parameters involved:

$$\frac{H_1}{W} = c_1(R_G)R_f^{\,m_1(R_G,\lambda)}R_p^{\,n_1(R_G)}\,; \tag{XV.14}$$

$$\frac{H_2}{W} = c_2(R_G)R_f^{\,m_2(R_G,\lambda)}R_p^{\,n_2(R_G)}\,. \tag{XV.15}$$

Following are the procedures we used to achieve the bi-power correlations: (1) Different kinds of proppant and fluid are used in bed load transport experiments and lead to different values of R_G and λ. For each single case, we develop bi-power law correlations of H_1 and H_2. (2) The prefactors and exponents in these correlations are functions of R_G and λ. We implement curve-fitting to find analytical expression for these coefficients. (3) Curve fitting implies that c_1, n_1, c_2 and n_2 can be reasonably approximated by logarithmic functions of R_G. While the trend of m_1, m_2 is less obvious. (4) We use the predicted c_1, n_1, c_2, *and n2* by the logarithmic functions of R_G and vary m_1, m_2 in the bi-power law correlations to match the measured H_1 and H_2 consistently. The new m_1 and m_2 turn out to be also logarithmic functions of R_G, but with slopes and intercepts as functions of λ. (5) With the explicit and analytical expressions for all the coefficients in the bi-power law known: $c_1(R_G)$, $c_2(R_G)$, $n_1(R_G)$, $n_2(R_G)$, $m_1(R_G, \lambda)$, $m_2(R_G, \lambda)$, we predict H_1 and H_2 and compare them with the experimentally measured values. The analytical expressions $c_1(R_G)$, $c_2(R_G)$, $n_1(R_G)$, $n_2(R_G)$, $m_1(R_G, \lambda)$ and $m_2(R_G, \lambda)$ can be adjusted to obtain the best fit for H_1 and H_2. Hence, we obtain the final form for the analytical expressions: (XV.16) –

(XV.21). Then they are inserted to (XV.14) and (XV.15), giving rise to (XV.22) and (XV.23) as the final form for the bi-power law correlations.

Next, we present the analytical expressions for the prefactors and exponents in the bi-power law correlations. These expressions are plotted in figure XV.6–XV.9.

$$c_1 = -0.000230175\ln(R_G) + 0.0029193 ; \qquad \text{(XV.16)}$$

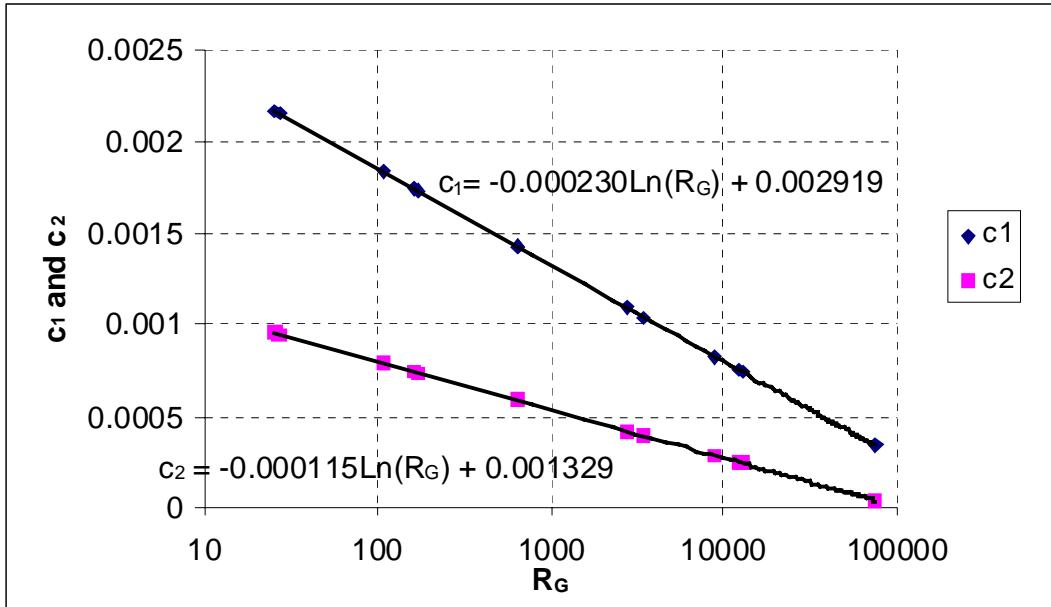$$c_2 = -0.000114966\ln(R_G) + 0.001328763 ; \qquad \text{(XV.17)}$$

Figure XV.6. Prefactors c_1 *and* c_2 *as logarithmic functions of* R_G.

$$n_1 = -0.01720815\ln(R_G) - 0.12002233 ; \qquad \text{(XV.18)}$$

$$n_2 = -0.0071596\ln(R_G) - 0.3041344 . \qquad \text{(XV.19)}$$
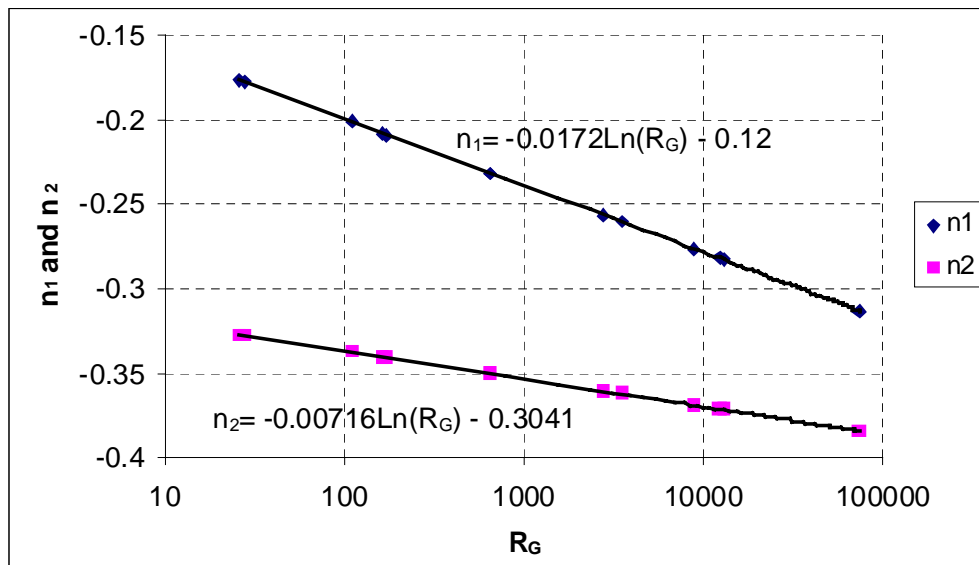
Figure XV.7. Exponents n_1 *and* n_2 *as logarithmic functions of* R_G.

$$m_1 = 1.2 - 0.001257\,\lambda^{-0.42785}\left[15.2 - \ln(R_G)\right] \qquad \text{(XV.20)}$$
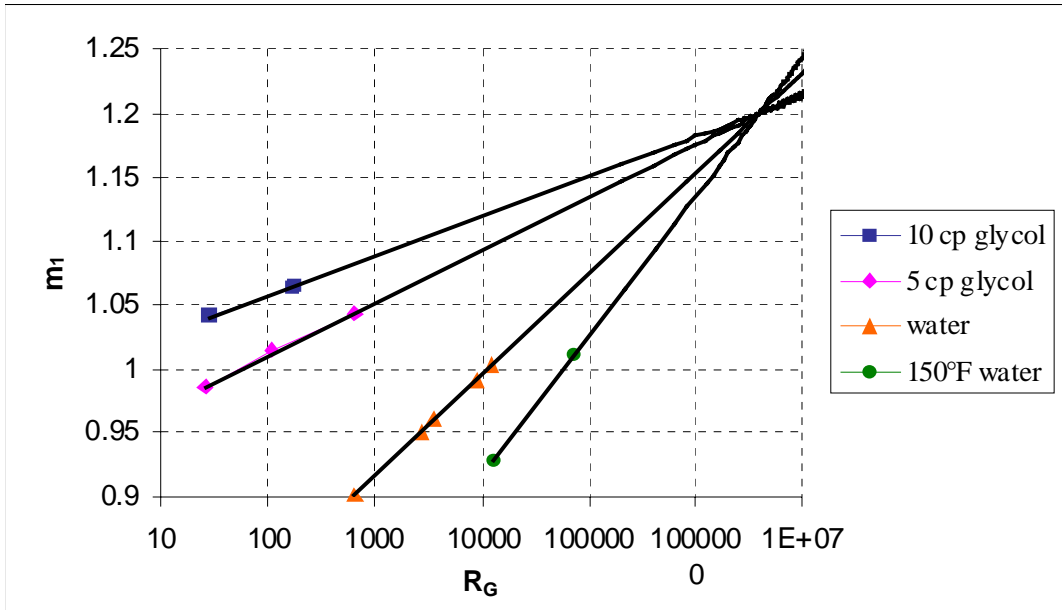
Figure XV.8. Exponent m_1 *as a logarithmic function of* R_G *with the slopes and intercepts as functions of* λ.

$$m_2 = 1.2012713 - 1.295\times10^{-6}\,\lambda^{-1.28089}\left[11.667387 - \ln(R_G)\right] \qquad \text{(XV.21)}$$
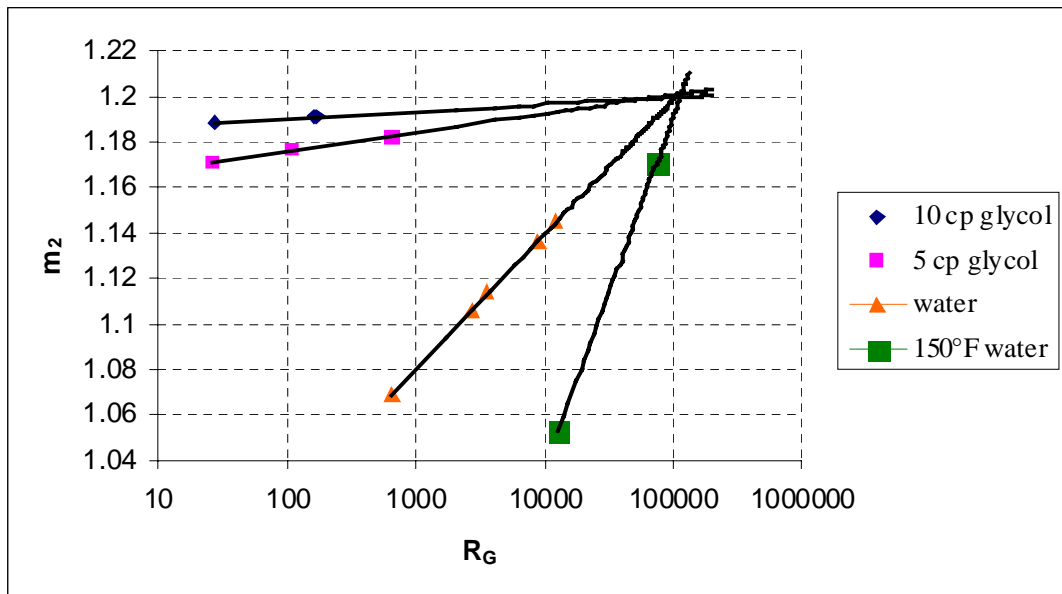
Figure XV.9. Exponent m_2 *as a logarithmic function of* R_G *with the slopes and intercepts as functions of* λ.

From figure XV.6–XV.9, we can see that c_1, n_1, c_2 and n_2 can be represented by logarithmic functions of R_G, while m_1 and m_2 are logarithmic functions of R_G with slopes and intercepts as functions of λ. Equation (XV.20) implies that for any λ, the logarithmic curve $m_1(R_G, \lambda = \text{constant})$ passes through the point (m_1=1.2, $\ln(R_G)$=15.2). Equation (XV.21) shows that such

a point for $m_2(R_G, \lambda)$ is (m_2=1.201, $ln(R_G)$=11.67). In figure XV.8 and XV.9, we can see the two points.

In table XV.4, the bed load transport experiments with the corresponding R_G and λ are listed. Note that the proppant and fluid used in these experiments and their properties can be found in the table XV.B2. c_1, c_2, m_1, m_2, n_1 and n_2 listed in table XV.4 are predicted by (XV.16)–(XV.21) corresponding to R_G and λ listed in the first and second columns. These c_1, c_2, m_1, m_2, n_1 and n_2 have been plotted in figure XV.6–XV.9, indicated by points.

R_G	λ	c_1	c_2	n_1	n_2	m_1	m_2
27.51	0.00396	0.002156	0.000999	-0.1771	-0.33101	1.04072	1.18938
162.2879	0.00396	0.001751	0.000781	-0.2074	-0.34528	1.064336	1.192695
172.895567	0.00396	0.001733	0.000772	-0.2087	-0.3459	1.065354	1.192838
25.8172784	0.002034	0.002171	0.001007	-0.176	-0.3305	0.987032	1.168948
107.151931	0.002034	0.001843	0.000831	-0.2005	-0.34202	1.012398	1.175391
643.994554	0.002034	0.001431	0.000609	-0.2313	-0.35655	1.044363	1.18351
648.07	0.000452	0.001429	0.000608	-0.2314	-0.3566	0.90401	1.057401
2818.38293	0.000452	0.001091	0.000426	-0.2567	-0.3685	0.953871	1.105684
3496.28	0.000452	0.001041	0.000400	-0.2604	-0.37025	0.961182	1.112763
8903.2	0.000452	0.000826	0.000284	-0.2765	-0.37781	0.992887	1.143466
15921.522	0.000452	0.000692	0.000212	-0.2865	-0.38252	1.012604	1.162559
12755.3536	0.000209	0.000743	0.00024	-0.2827	-0.38073	0.929031	1.070145
73483.2936	0.000209	0.00034	2.31E-05	-0.3128	-0.39491	1.011605	1.228776

Table XV.4: R_G and λ for bed load transport experiments and the corresponding c_1, c_2, m_1, m_2, n_1 and n_2 predicted by (XV.16)–(XV.21).

Inserting the analytical expressions (XV.16)–(XV.21) into (XV.14) and (XV.15), we get the final form for the bi-power law correlations:

$$\frac{H_1}{W} = [-0.000230\ln(R_G) + 0.00292]R_f^{1.2-0.00126\lambda^{-0.428}[15.2-\ln(R_G)]}R_p^{[-0.0172\ln(R_G)-0.120]}, \quad \text{(XV.22)}$$

$$\frac{H_2}{W} = [-0.000115\ln(R_G) + 0.00133]R_f^{1.2-1.295\times10^{-6}\lambda^{-1.28}[11.67-\ln(R_G)]}R_p^{[-0.0072n(R_G)-0.304]}. \quad \text{(XV.23)}$$

We emphasize that equations (XV.22) and (XV.23) are explicit and predictive correlations for proppant transport. By (XV.22) and (XV.23), H_1 and H_2 can be predicted from the prescribed parameters: ρ_f, ρ_p, d, η, W, Q_p, Q_f.

We predict H_1/W and H_2/W by (XV.22) and (XV.23). In figure XV.10 and XV.11, we plot the predicted *values* against the experimentally measured data. Ideally, all the points should be on the straight-line $y=x$. It can be seen that the predicted values are in good agreement with the experimental data.
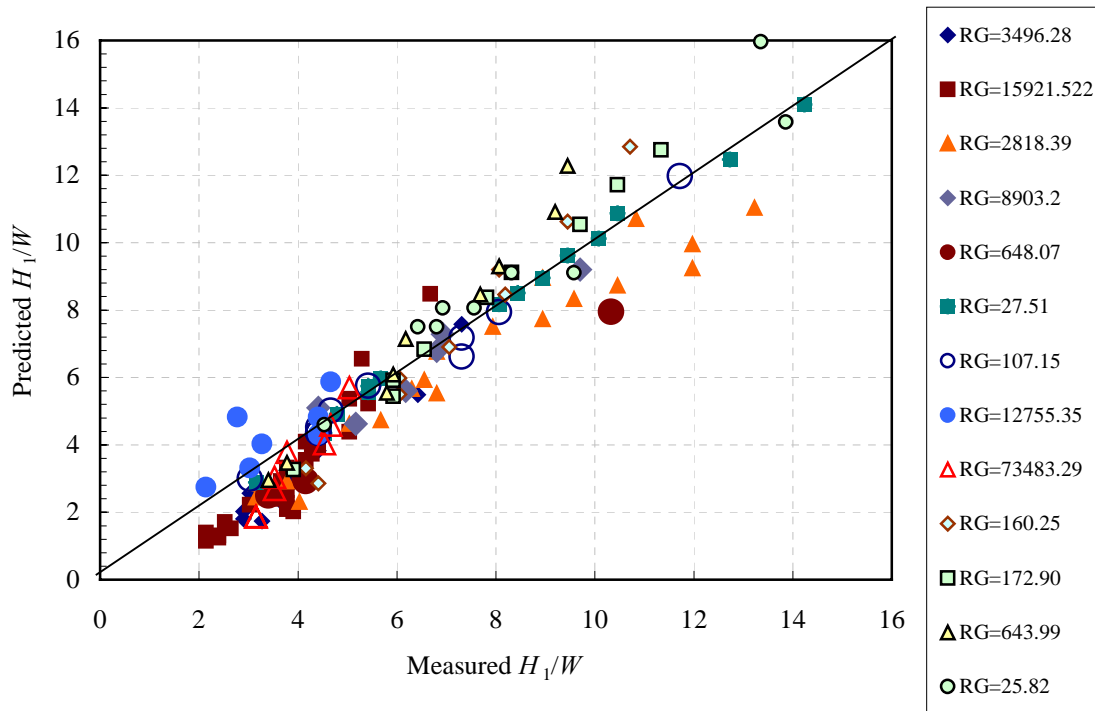
Figure XV.10. The predicted values of H_1/W *by equation (XV.22) versus the experimentally measured values for the cases listed in table XV.4.*
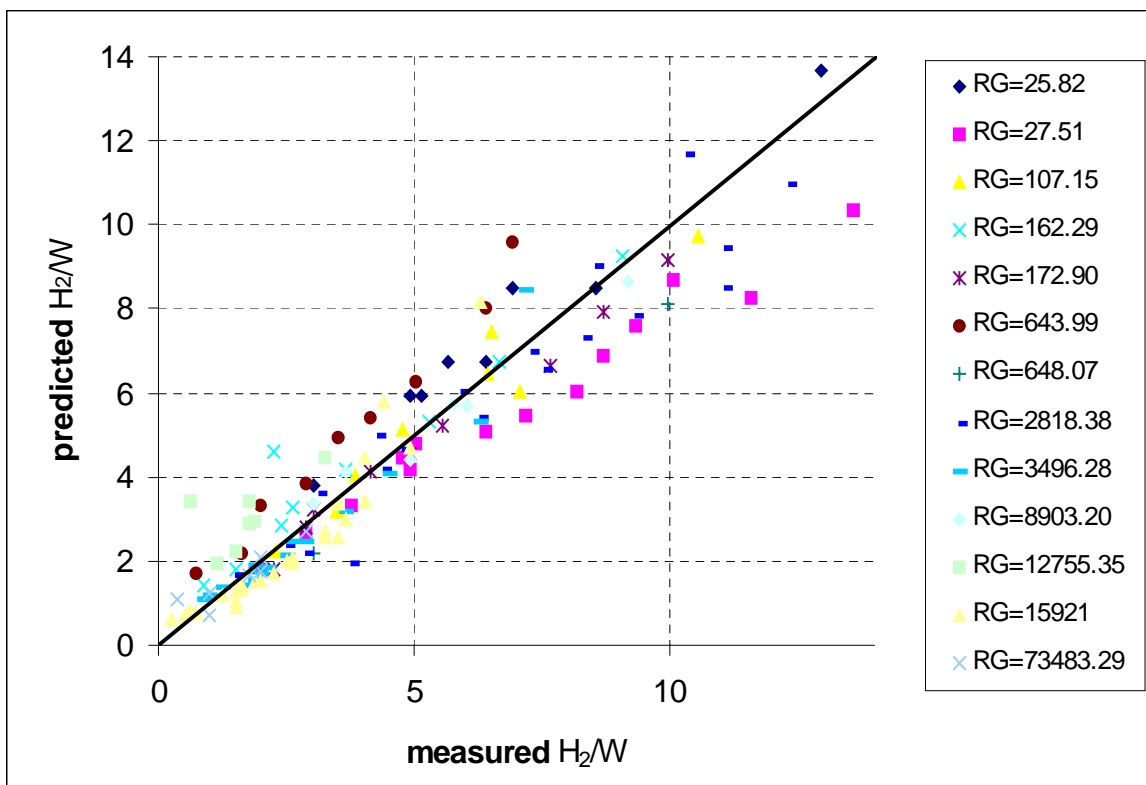

Figure XV.11. The predicted values of H_2/W *by equation (XV.23) versus the experimentally measured values for the cases listed in table XV.4.*

To test this correlation, experiments were conducted in the slot which is 16 feet long and 4 feet high. (Note that the correlations are extracted from experiments conducted in the slot which is 8 feet long and 1 foot high.) Following are the prescribed parameters for the experiments in the 16-foot-long slot: 20/40 Ottawa with water, ρ_f : 0.997gm/cc, ρ_p : 2.645gm/cc, d: 0.0548cm, η: 0.00998poise, W : 0.79375cm, R_G: 2663.189, λ: 0.000452.

R_f	Rp	Predicted H_1/W	Predicted H_2/W	Predicted H_1(cm)	Predicted H_2(cm)	Measured H_1(cm)	Measured H_2(cm)
514437.8	14327.87	28.81	25.79502	22.86977	20.4748	24.5	24.30
570181.8	38207.65	24.73	20.14101	19.62663	15.98693	20.2	19.2

Table XV.5. The predicted H_1 and H_2 in comparison with the measured H_1 and H_2 in experiments conducted in the slot which is 16 feet long and 4 feet high.

We can see that the agreement between predicted values and measured values is encouraging. We believe that our correlation provides a promising way to predict transport of proppant.

3.4 Logistic dose curve fitting for H_1/W and H_2/W

The bi-power law correlation gives good prediction of H_1/W and H_2/W for the bed load transport case. However, it is not compatible with the erosion case. When R_p approaches zero, H_1/W and H_2/W tend to infinity. Therefore we need a different correlation to account for the transition region from the erosion case to the bed load transport case.

We fit the data for H_1/W and H_2/W to a logistic dose curve (see Appendix A for details) to determine a function valid in the transition region; this fitting effectively combines the power law for the erosion case and the bi-power law for the bed load transport case. We seek to determine the function:

$$\frac{H_1}{W} = C_1 R_f^{M_1} \frac{1}{(1 + \frac{R_p}{T_1})^{N_1}} \tag{XV.24}$$

and

$$\frac{H_2}{W} = C_2 R_f^{M_2} \frac{1}{(1 + \frac{R_p}{T_2})^{N_2}} . \tag{XV.25}$$

When R_p=0 (the erosion case), (XV.24) and (XV.25) reduce to:

$$\frac{H_1}{W} = C_1 R_f^{M_1} , \tag{XV.26}$$

$$\frac{H_2}{W} = C_2 R_f^{M_2} . \tag{XV.27}$$

For the erosion case, $H = H_1 = H_2$; hence, $C_1=C_2$, $M_1=M_2$ and we recover the power law correlation (XV.13) for the erosion case. When $R_p>>T_1$ and $R_p>>T_2$, (XV.24) and (XV.25) reduce to:

$$\frac{H_1}{W} = (C_1 T_1^{N_1}) R_f^{M_1} R_p^{-N_1} \quad, \tag{XV.28}$$

$$\frac{H_2}{W} = (C_2 T_2^{N_2}) R_f^{M_2} R_p^{-N_2} . \tag{XV.29}$$

Therefore, we recover the bi-power law correlations (XV.14) and (XV.15) for the bed load transport case.

Comparing (XV.28) and (XV.29) to (XV.14) and (XV.15), we observe that M_1 and M_2 should be functions of both R_G and λ; hence, the exponent $M_1=M_2$ in the power law correlations for the erosion case should be functions of R_G and λ. However, most of the erosion experiments were conducted using water at different temperatures and lead to a small range of λ (See table XV.B1); we do not have enough data to find an analytical expression $M_1(R_G, \lambda)=M_2(R_G, \lambda)$. However, we find that $C_1, M_1, T_1, N_1, C_2, M_2, T_2$ and N_2 can be reasonably approximated by functions of a single variable R_G; hence, the coefficients in (XV.24) and (XV.25) are functions of R_G only.

We do not have data for erosion and bed load transport with the same R_G (See table XV.B1 and XV.B2) so that we use (XV.24) and (XV.25) to fit data from erosion and bed load transport with different but close R_G:

1: Erosion case with R_G=86 and bed load transport case with R_G=109,
2: Erosion case with R_G=521 and bed load transport case with R_G=648,
3: Erosion case with R_G=2290 and bed load transport case with R_G=2761,
4: Erosion case with R_G=13363,14513 and bed load transport case with R_G=12229.

The results of fitting erosion with R_G=86 and bed load transport with R_G=109 are presented below:

$$\frac{H_1}{W} = 0.007846 R_f^{0.748778} \frac{1}{(1+\frac{R_p}{68.23195})^{0.11166}}, \quad (\sigma^2 = 0.951) \tag{XV.30}$$

$$\frac{H_2}{W} = 0.007846 R_f^{0.748778} \frac{1}{(1+\frac{R_p}{59.2391})^{0.155747}}, \quad (\sigma^2 = 0.946) \tag{XV.31}$$

By (XV.30) and (XV.31), H_1/W and H_2/W are computed and tabulated in table XV.6.

R_G	R_f	R_p	H_1/W	H_2/W	computed H_1/W	error	computed H_2/W	error
86.83778	897.05	0	1.76378	1.76378	1.275422	0.238493	1.275422	0.238493
86.83778	1184.19	0	2.519685	2.519685	1.570219	0.901486	1.570219	0.901486
86.83778	3631.42	0	4.913386	4.913386	3.633766	1.637427	3.633766	1.637427
86.83778	14611.89	0	10.70866	10.70866	10.30601	0.162123	10.30601	0.162123
86.83778	25735.84	0	15.11811	15.11811	15.74579	0.393979	15.74579	0.393979
109.48	5202.438	570.7087	2.863739	2.301595	3.704969	0.707668	3.291238	0.979393
109.48	17341.46	1902.362	8.183906	7.060129	8.047953	0.018483	6.792796	0.071467
109.48	8670.73	95.1182	7.229334	6.502897	6.324757	0.818258	6.006224	0.246684

(continued)

109.48	8670.73	142.6773	7.168748	6.437499	6.146838	1.044302	5.76016	0.458789
109.48	8670.73	285.3543	5.53511	4.795559	5.802219	0.071347	5.300052	0.254513
109.48	8670.73	570.7087	4.594431	3.846482	5.431254	0.700274	4.82475	0.957008
109.48	8670.73	951.1811	4.282596	3.528398	5.155187	0.761415	4.482455	0.910225
109.48	8670.73	1141.417	4.220726	3.464284	5.057626	0.700402	4.36363	0.808822
109.48	8670.73	1141.417	4.283718	3.527276	5.057626	0.598934	4.36363	0.699488
109.48	26012.19	1902.362	11.9804	10.57071	10.90282	1.161175	9.202417	1.872216

Table XV.6: Data structure for the combination of erosion case with $R_G=86$ and bed load transport case with $R_G=109$. H_1/W and H_2/W calculated by equation (XV.30) and (XV.31) are listed in comparison with the experimentally measured values. The error is computed by (calculated value - measured value)^2.
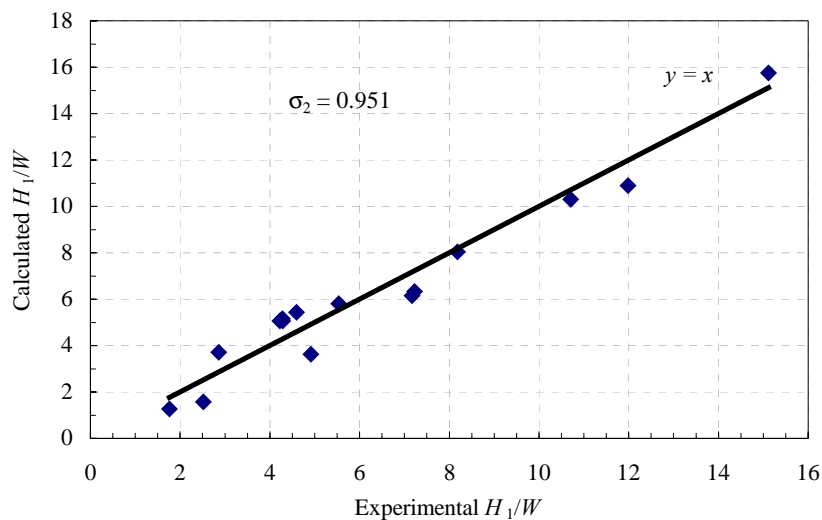
Figure XV.12(a): Experimental H_1/W vs. calculated H_1/W using (XV.30).
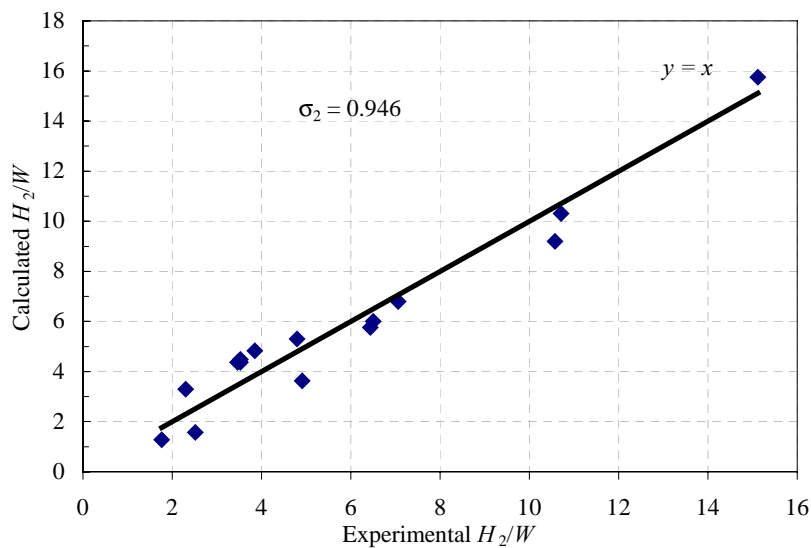
Figure XV.12(b): Experimental H_2/W vs. calculated H_2/W using (XV.31).

We can see that the computed H_1/W and H_2/W are in good agreement with the experimentally observed values. Cases 2, 3 and 4 are processed in the same manner and resultant coefficients C_1, M_1, T_1, N_1, C_2, M_2, T_2, N_2 and σ-squared values are listed in table XV.7.

R_G	C_1	M_1	T_1	N_1	σ^2	C_2	M_2	T_2	N_2	σ^2
109.48	0.007846	0.748778	68.232	0.112	0.951	0.007846	0.748778	59.2391	0.155747	0.946
648.1	0.000856	0.923591	4.173	0.190	0.987	0.000856	0.923591	31.60245	0.319314	0.981
2761.9	0.000184	1.080253	3.332	0.234	0.964	0.000184	1.080253	9.694597	0.299927	0.929
12229	8.94E-06	1.361329	0.174	0.133	0.9453	8.94E-06	1.361329	5.008106	0.278326	0.9448

Table XV.7: The coefficients in the logistic dose curve fitting of H_1/W *and* H_2/W *for the data from erosion and bed load transport with close* R_G*. We only list the* R_G *of the bed load transport case in the first column.*

Next we obtain the functions $C_1(R_G)$, $M_1(R_G)$, $T_1(R_G)$, $N_1(R_G)$, $C_2(R_G)$, $M_2(R_G)$, $T_2(R_G)$, and $N_2(R_G)$.
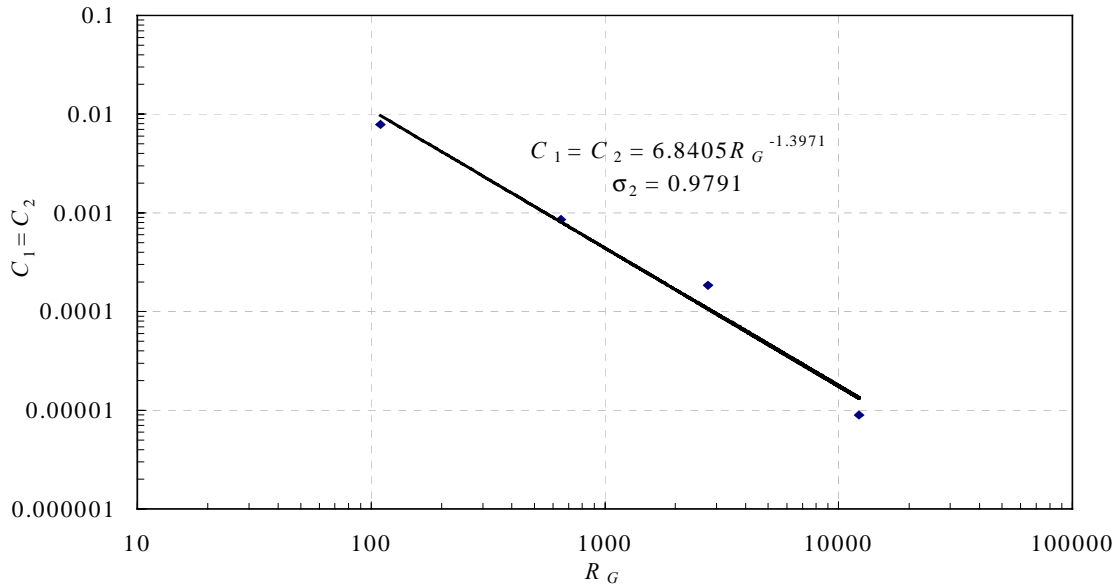
Figure XV.13: The coefficient $C_1 = C_2$ *as a function of* R_G.

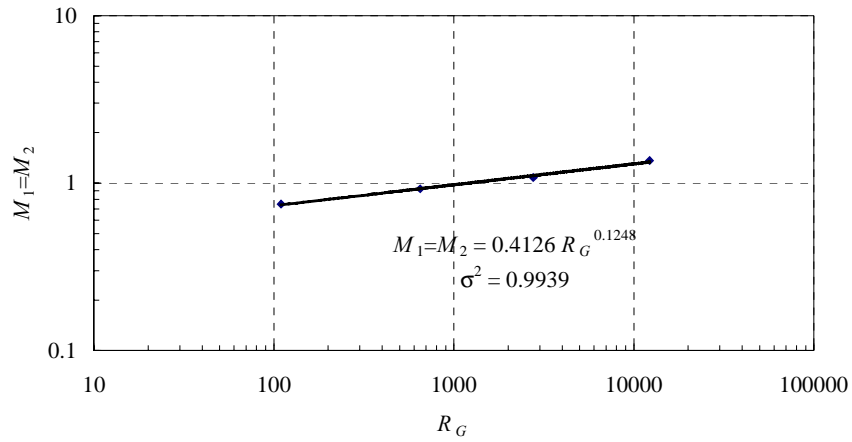$$C_1 = C_2 = 6.8405 R_G^{-1.3971}, \quad (\sigma^2 = 0.9791) \qquad (XV.32)$$

Figure XV.14: The coefficient $M_1 = M_2$ *as a function of* R_G.
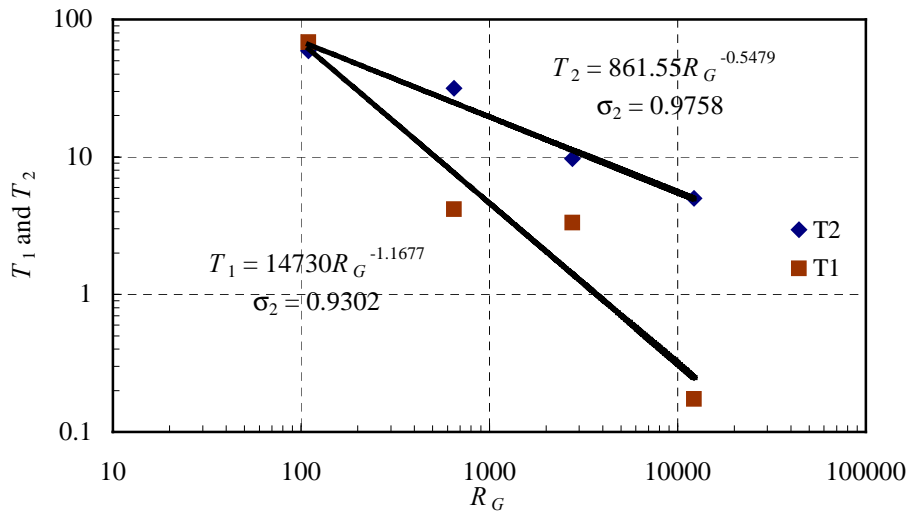
$$M_1 = M_2 = 0.4126 R_G^{0.1248} \quad . \tag{XV.33}$$
$$(\sigma^2 = 0.9939)$$

Figure XV.15: The coefficient T_1 *and* T_2 *as functions of* R_G.

$$T_1 = 14730 R_G^{-1.1677} \; ; \;\; (\sigma^2 = 0.9302) \tag{XV.34}$$

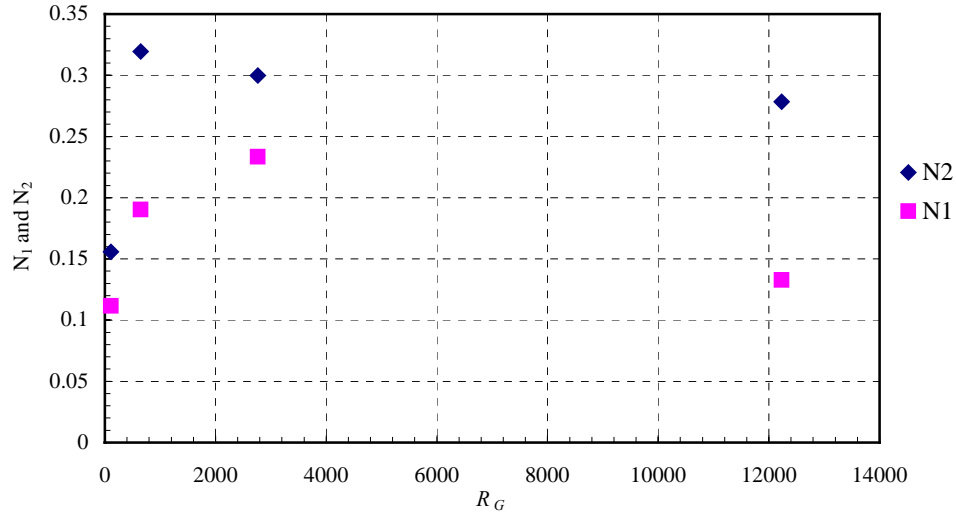$$T_2 = 861.55 R_G^{-0.5479} \; , \;\; (\sigma^2 = 0.9758). \tag{XV.35}$$

Figure XV.16: The coefficient N_1 *and* N_2 *plotted against* R_G.

We use a natural cubic spline to interpolate $N_1(R_G)$ and $N_2(R_G)$ and the results are plotted in figure XV.17. Because we do not have enough data, the spline interpolation is not reliable and could be siginificantly changed when more data become available.
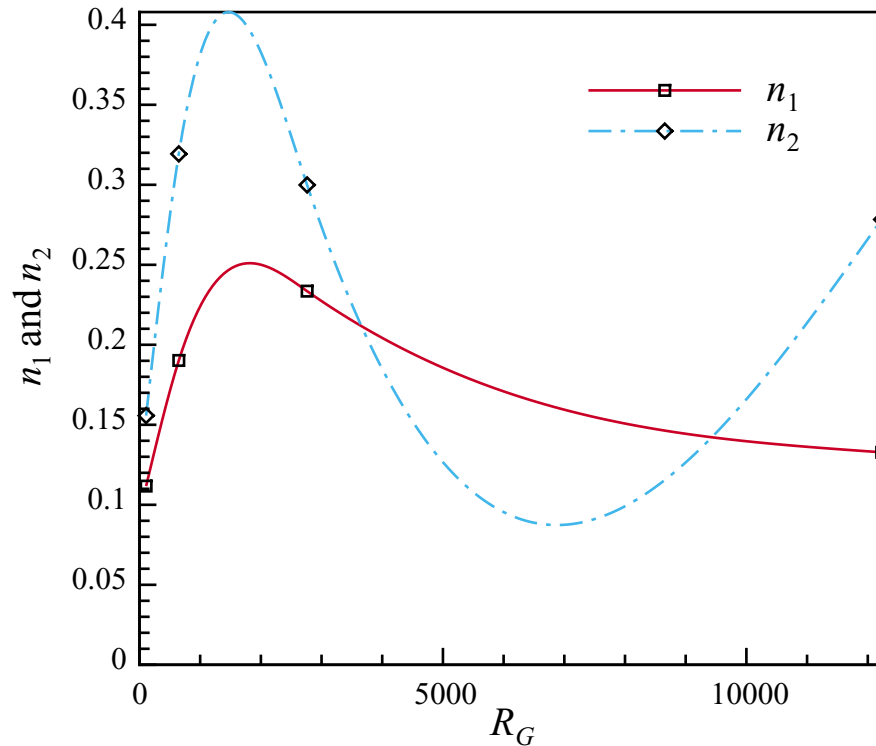

Figure XV.17. Use natural cubic spline to interpolate $N_1(R_G)$ *and* $N_2(R_G)$.

The resultant expressions of the spline interpolation are:

$$N_1 = A_1 + B_1 R_G + C_1 R_G^2 + D_1 R_G^3 \qquad \text{(XV.36)}$$

where the values of A_1, B_1, C_1, D_1 are listed in the following table:

Range	109.48—648.1	648.1—2761.9	2761.9—12229
A_1	9.4344824626E-02	7.9038758235E-02	3.2815903993E-01
B_1	1.5713752027E-04	2.2798800770E-04	-4.2608636465E-05
C_1	1.4612470982E-08	-9.4707834681E-08	3.2669847295E-09
D_1	-4.4490532619E-11	1.1735517774E-11	-8.9050201147E-14

Table XV.8: The coefficients in the spline intopolation for $N_1(R_G)$.

$$N_2 = A_2 + B_2 R_G + C_2 R_G^2 + D_2 R_G^3 \qquad (XV.37)$$

where the values of A_2, B_2, C_2, D_2 are listed in the following table:

Range	109.48—648.1	648.1—2761.9	2761.9—12229
A_2	1.1903363556E-01	7.9383985185E-02	7.6244366512E-01
B_2	3.3261384535E-04	5.1614872518E-04	-2.2579671537E-04
C_2	3.7393518981E-08	-2.4579562890E-07	2.284026181E-08
D_2	-1.1385189939E-10	3.1799059083E-11	-6.2257098948E-13

Table XV.9: The coefficients in the spline intopolation for $N_2(R_G)$.

The final correlations:

$$\frac{H_1}{W} = 6.8405 R_G^{-1.3971} R_f^{0.4126 R_G^{0.1248}} \frac{1}{(1 + \frac{R_p}{14730 R_G^{-1.1677}})^{N_1(R_G)}} \;, \qquad (XV.38)$$

$$\frac{H_2}{W} = 6.8405 R_G^{-1.3971} R_f^{0.4126 R_G^{0.1248}} \frac{1}{(1 + \frac{R_p}{861.55 R_G^{-0.5479}})^{N_2(R_G)}} \qquad (XV.39)$$

where $N_1(R_G)$ and $N_2(R_G)$ are expressed in (30) and (31).

Correlations (XV.38) and (XV.39) can be used to predict H_1/W and H_2/W with the prescribed parameters W, ρ_f, ρ_p, d η, Q_f and Q_p. These correlations are compatible with both the power law for the erosion case and the bi-power law for the bed load transport case.

We developed the logistic dose curve by fitting the data for erosion and bed load transport using equation (XV.24) and (XV.25). The curve should depend on R_G and λ but we do not have enough data to determine how it depends on λ. This fitting using the dose curve is independent of the previous power law and bi-power law correlations and the resultant equation (XV.38) and (XV.39) do not reduce precisely to equation (XV.13), (XV.22) and (XV.23) at the respective limits. We emphasize that the logistic dose curve represents a correlation for transition situations between erosion and bed load transport; it is not as accurate as the power law (XV.5) for erosion or the bi-power law (XV.22) and (XV.23) for bed load transport.

▪ **Summary**

We believe that research leading to optimal techniques of processing data for correlations from real and numerical experiments is founded on the far from obvious property of self similarity (power laws) in the flow of dispersions. The basis for this belief are the excellent

correlations of experiments on fluidization and sedimentation done by Richardson & Zaki and the correlations for sediment transport in horizontal channels obtained from our numerical simulations and the analysis of the experimental data from STIM-LAB.

Results of two dimensional simulations of solid-liquid flows give rise to straight lines in log-log plots of the relevant dimensionless Reynolds numbers. Power laws are also obtained from the analysis of experimental data. The extent and apparent universality of this property is remarkable and shows that the flow of these dispersions are governed by a hidden property of self similarity leading to power laws. These power laws make a powerful connection between sophisticated high performance computation, experiments and the world of engineering correlations.

The correlations obtained can be used as predictive tools or as a basis for models for sediment transport in simulators used for design purposes.

In a sense our results here realize the opportunity which is presented by digital technology for implementing the old tried and true method of correlations to big data sets. Our mantra is "the secrets are in the data." The same method works well for data from numerical and from real experiments. We have used the following procedure not only for this but also for other multiphase flow processes. First we propose candidates for controlling dimensionless parameters and list the data required to form these numbers in a spreadsheet. Then we identify two parameters and plot the results of the experiments for those two in log-log plots under conditions in which other parameters are fixed. We have a good choice when the plots come up as straight lines in the log-log plot. Here and elsewhere we have had excellent results in this search using the parameters suggested by making the governing sets of PDE's dimensionless. The results of this kind of power law processing is that the slopes and intercepts of the straight lines in log-log plots, or the prefactors and exponents of the power laws these lines imply, depend on the parameters we have fixed. When we look at the variation of these parameters, the prefactors and exponents sometimes are expressible as power laws and sometimes they are not. In any case we may and do implement curve-fitting procedures for the prefactors and exponents to present explicit formulas in analytic form for the prediction of future events.

We might add that the search for the governing dimensionless numbers in multiphase flow is a way to achieve a deep understanding of the underlying physics. The method of correlations is an excellent procedure to guide the research because the data doesn't lie.

▪ Appendix A (contribution of B. Baree)

Fitting power-law data with transition regions by a continuous function: General framework and application to the Richardson-Zaki correlation

Many data sets representing naturally occurring phenomena can be described using a Sigmoidal distribution function. One such function that is particularly useful in fitting physical data is the logistic dose response curve given by:

$$y = a + \frac{(b-a)}{\left(1+\left(\dfrac{x}{t}\right)^{c}\right)^{d}} \qquad\qquad (XV.A1)$$

In this equation each of the constant terms or coefficients (*a, b, c, d* and *t*) have readily apparent physical significance, which allows data modeling to be accomplished almost by inspection.
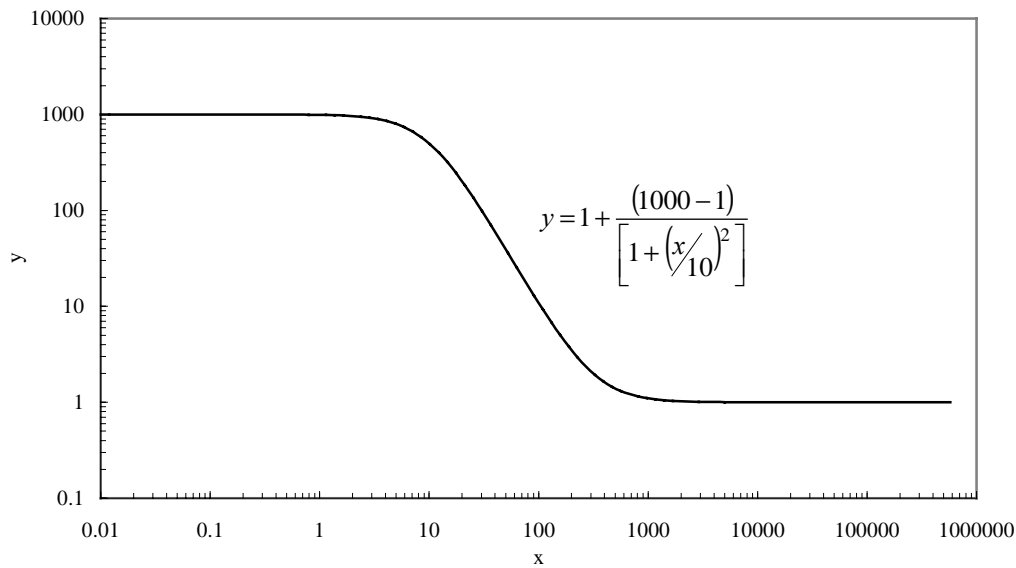
Figure XV.A1. A typical logistic dose response curve.

Figure XV.A1 shows the dose-response function for $a = 1$, $b = 1000$, $c = 2$, $d = 1$, and $t = 10$. As can be seen, the coefficients a and b represent the values of the lower and upper plateaus of the function, respectively, or its range. The coefficient t defines the value of the independent variable (x) where the function deviates from the constant first plateau value. The sharpness of curvature during the deviation from the first plateau is determined by the coefficient c. The slope of the power-law straight line in transition from the first plateau to the second plateau is determined by the product of coefficients c and d. The slope in this example is negative because both exponents are positive in the denominator of the rational fraction.
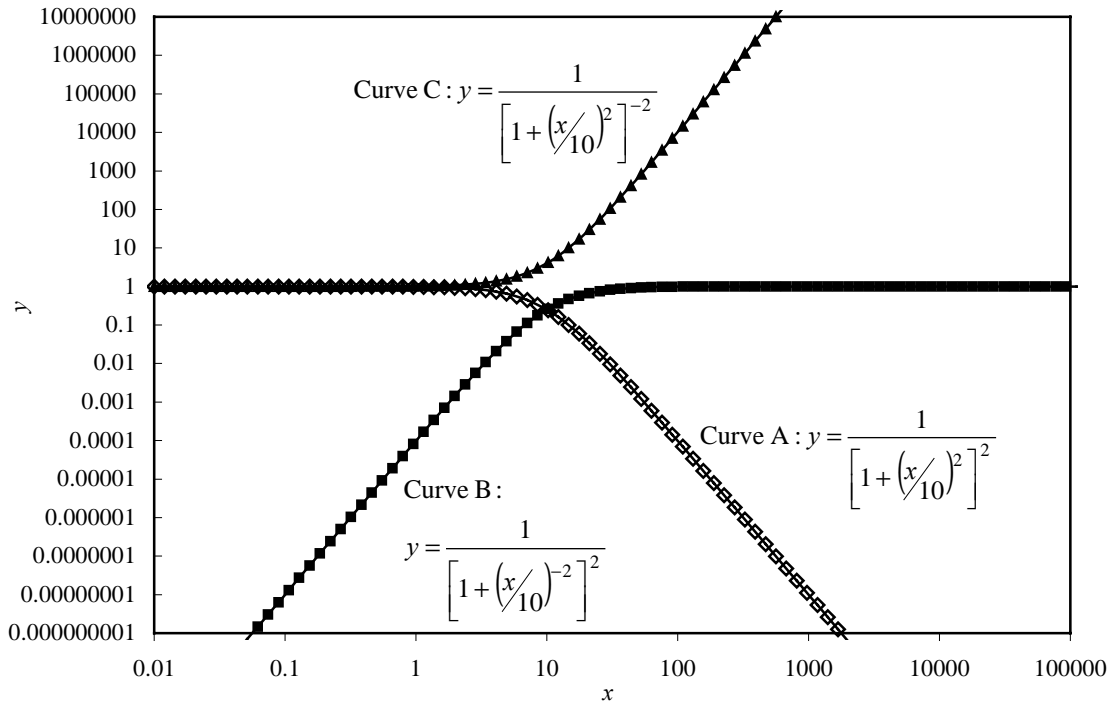
Figure XV.A2. Effects of changing signs of coefficients c and d in the logistic dose response curve.

The effects of changing the signs of the exponents can be examined (figure XV.A2). If the sign of coefficient *c* is changed, the plot is essentially rotated about a line parallel to the y-axis through the transition value *t* (compare curves A and B in figure XV.A2). If the sign of the coefficient *d* is changed, the plot is rotated about a line parallel to the x-axis through the upper bound *b* (compare curves A and C in figure XV.A2). These relationships allow construction of a transition function in any general form. Another useful property of this function is that the bound corresponding to the coefficient *a* can be eliminated by setting its value to zero. With $a = 0$ the function yields a horizontal line at the upper bound value *b* and a power-law line of slope $c{\times}d$ which extends to infinity (Curve A, figure XV.A2). Various functions can then be modeled by products of functions with specified power-law slopes and transition points (figure XV.A3). For curve A in figure XV.A3 $c_1 = 2$, $d_1 = 1$ and for curve B $c_2 = 1.6$, $d_2 = -1$. The final power-law slope in the product is then $c_1{\times}d_1 + c_2{\times}d_2$.
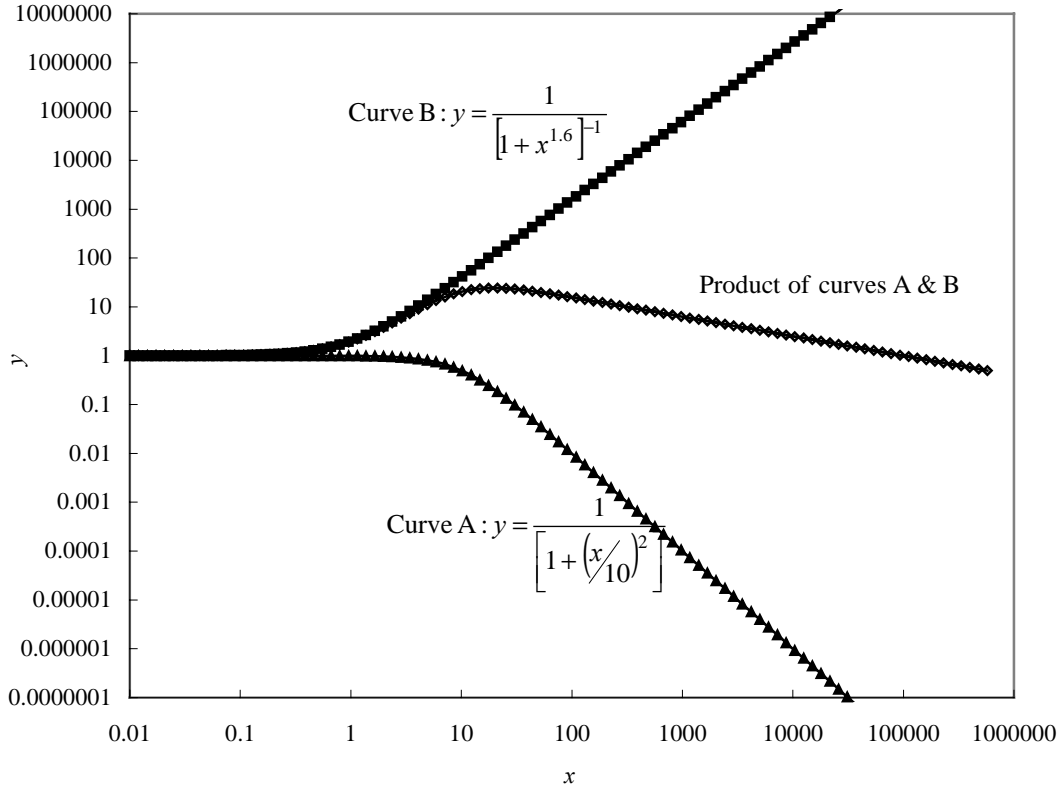
Figure XV.A3. Obtaining a curve from the product of two different logistic dose response curves.

Combinations of these functions can be used in various forms to model many commonly observed phenomena. The logistic dose response curve can also be multiplied by a linear power law function to impose an overall slope to the function. Quite complex systems can be modeled by combining rational fractions or products of multiple functions.

This method has been used to model the Richardson-Zaki correlation that relates bed fluidization velocity to the solids volume-fraction of particles in suspension. The Richardson-Zaki correlation is given by (XV.1). Specifically, the various functions representing the exponent *n* are (Richardson & Zaki, 1954)

$$n = \left(4.65 + 19.5 \frac{d}{D} \right) \quad when \quad R_0 < 0.2;$$

$$n = \left(4.35 + 17.5 \frac{d}{D} \right) R_0^{-0.03} \quad when \quad 0.2 < R_0 < 1;$$

$$n = \left(4.45 + 18 \frac{d}{D} \right) R_0^{-0.1} \quad when \quad 1 < R_0 < 200 \qquad (XV.A2)$$

$$n = 4.45 R_0^{-0.1} \quad when \quad 200 < R_0 < 500;$$

$$n = 2.39 \quad when \quad 500 < R_0$$

In these relations *d* is particle diameter, and *D* is the diameter of the fluidization column. Note that in (XV.A2) the value of *n* at the transition points is not unique. Nevertheless, these

functions can be replaced with a single continuous form of the logistic dose response curve where R_0 is the independent variable and n is the dependent result (figure XV.A4).
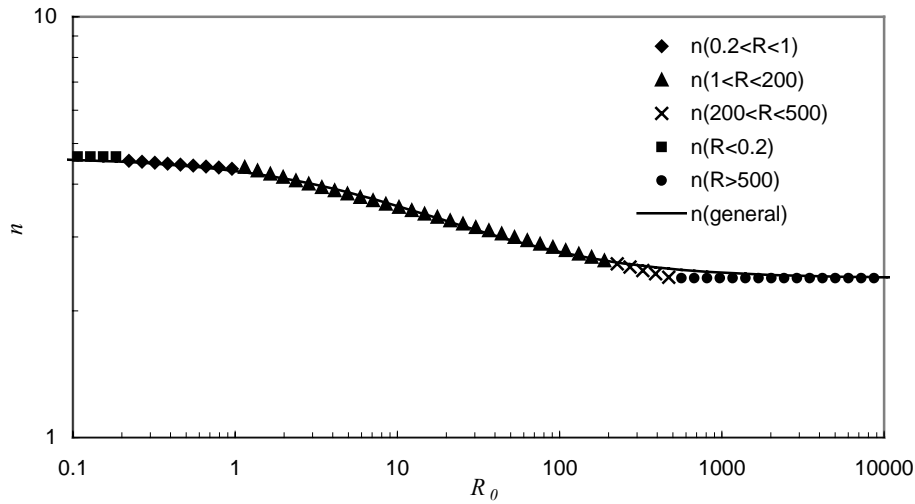

Figure XV.A4. A continuous logistic dose response curve for the Richardson-Zaki exponent n for d/D = 0.

Figure XV.A4 shows a continuous curve for the Richardson-Zaki exponent n. The continuous form of the function is formed assuming that n should not decrease below a value of 2.39 for any value of Re. The continuous form is generated by the equation

$$n = 2.39 + \frac{\left(2.26 + 19.5 \frac{d}{D}\right)}{\left[1 + \left(\frac{R_o}{T}\right)^{0.7}\right]^{1.1}}$$ (XV.A3)

This function sets a minimum value of $n = 2.39$ and a maximum that is a function of the ratio of particle size to vessel diameter (first of (XV.A2)). The transition value T is also a weak function of the diameter ratio d/D, and is given by

$$T = 1 + \frac{12.0}{\left(1 + \left(\frac{d/D}{0.1}\right)\right)}$$ (XV.A4)

The final calculation of n is then given by a combination of (XV.A3) and (XV.A4). Rowe 1987 obtained an empirical equation for the Richardson-Zaki exponent by using the logistic curve for $d/D = 0$. We verified that there is good quantitative agreement between (XV.A3) (for $d/D = 0$) and Rowe's equation.

Appendix B

Following tables give description to the proppant and fluid used in the erosion and bed load transport experiments.

Proppant	Fluid	ρ_f (gm/cc)	ρ_p gm/cc)	d (cm)	η (poise)	W (cm)	R_G	λ
60/4 Brady	water	0.999	2.65	0.0342	0.01115	0.79375	521.1554	0.000504
20/4 Ottawa	water	0.999	2.65	0.056	0.01115	0.79375	2290.846	0.000504
20/4 Light Beads	water	0.999	1.05	0.06	0.01115	0.79375	86.83778	0.000504
16/30Banrite	water	0.999	3.45	0.0884	0.01115	0.79375	13363.8	0.000504
12/20Badger	water	0.998	2.65	0.109	0.01015	0.79375	20342.67	0.000459
16/20 Carbolite	water	0.998	2.73	0.0949	0.01	0.79375	14513.68	0.000452
16/20 Carbolite	180 °F water	0.972	2.73	0.0949	0.00378	0.79375	100415.5	0.000176

Table XV.B1: Proppant and fluid parameters in erosion experiments.

Proppant	Fluid	ρ_f (gm/cc)	ρ_p gm/cc)	d (cm)	η (poise)	W (cm)	R_G	λ
20/40 sand	10cp glycol	1.11	2.645	0.0548	0.1	0.79375	27.50692	0.004067
16/30 ceramic	10cp glycol	1.14	2.73	0.097	0.1	0.79375	162.2879	0.003960
12/20 sand	10cp glycol	1.14	2.645	0.1009	0.1	0.79375	172.8956	0.003960
40/60 Sand	5cp glycol	1.11	2.645	0.0338	0.05	0.79375	25.81728	0.002034
20/40 sand	5cp glycol	1.11	2.73	0.097	0.05	0.79375	643.9946	0.002034
20/40 sand	5cp glycol	1.091	2.65	0.0548	0.05	0.79375	109.4829	0.002069
40/60 sand	water	0.997	2.65	0.0338	0.0098	0.79375	648.0661	0.000444
20/40 sand	water	0.997	2.65	0.0548	0.0098	0.79375	2761.919	0.000444
20/40 sand	water	1	2.65	0.06	0.01	0.79375	3496.284	0.000451
20/40 Bauxite	water	0.997	3.45	0.0709	0.0098	0.79375	8903.244	0.000444
16/30 Ceramic	water	1	2.71	0.09	0.01	0.79375	12229.05	0.000451
16/30 Ceramic	water	1	2.73	0.097	0.0098	0.79375	16127.91	0.000442
20/40 Sand	150 °F water	0.981	2.645	0.0548	0.004545	0.79375	12755.35	0.000209
16/30 Ceramic	150 °F water	0.981	2.73	0.097	0.004545	0.79375	74352.82	0.000209

Table XV.B2: Proppant and fluid parameters in bed load transport experiments.

(DISCARD THIS PAGE (only used to generate table of contents)